



Numerical and experimental assessment of liquid metal embrittlement in externally loaded spot welds

Konstantin Manuel Prabitz^{1,2,3} · Thomas Antretter³ · Michael Rethmeier^{4,5,6} · Bassel El-Sari⁵ · Holger Schubert⁷ · Benjamin Hilpert⁷ · Martin Gruber⁸ · Robert Sierlinger⁸ · Werner Ecker¹

Received: 13 November 2023 / Accepted: 22 January 2024
© The Author(s) 2024

Abstract

Zinc-based surface coatings are widely applied with high-strength steels in automotive industry. Some of these base materials show an increased brittle cracking risk during loading. It is necessary to examine electrogalvanized and uncoated samples of a high strength steel susceptible to liquid metal embrittlement during spot welding with applied external load. Therefore, a newly developed tensile test method with a simultaneously applied spot weld is conducted. A fully coupled 3D electrical, thermal, metallurgical and mechanical finite element model depicting the resistant spot welding process combined with the tensile test conducted is mandatory to correct geometric influences of the sample geometry and provides insights into the sample's time dependent local loading. With increasing external loads, the morphology of the brittle cracks formed is affected more than the crack depth. The validated finite element model applies newly developed damage indicators to predict and explain the liquid metal embrittlement cracking onset and development as well as even ductile failure.

Keywords Resistance spot welding · Finite element simulation · Advanced high-strength steel · Liquid metal embrittlement · Damage prediction · Tensile resistance spot welding experiment

1 Introduction

Resistance spot welding (RSW) is a critical manufacturing step for the formation of liquid metal embrittlement (LME)-induced cracks [1–3]. LME describes the intergranular

cracking mechanism of an otherwise ductile metal [4–6], which ultimately leads to the brittle fracture of the material. The occurrence of LME mainly depends on the loading parameters (temperature, plastic strain and rate of loading [7–10]) as well as on the material aspects, chemical composition, microstructure [6, 11, 12] and the galvanization process [8]. A prominent material class undergoing LME under certain conditions is galvanized third-generation advanced high-strength steels providing high ductility with an ultimate tensile strength (UTS) of 1000 MPa and higher. In the present article, an electrogalvanized (EG) and an uncoated (UC) dual-phase steel with a UTS of 1200 MPa and high ductility (DP1200HD) are investigated.

Uniaxial and isothermal hot tensile tests provide a simple and reproducible method to measure the susceptibility of a base material to LME [4, 13–18]. The susceptibility of a material to LME and proper welding parameters is measured during reproducible lab-scale welding experiments. The benefit of application-oriented laboratory RSW tests is the investigation of the whole welding system [19–21]. The electrode shape [22, 23], the welding schedule [1, 24–26] and many sorts of system interactions are naturally respected, while critical welding conditions for LME can

✉ Konstantin Manuel Prabitz
konstantin.prabitz@unileoben.ac.at

¹ Materials Center Leoben Forschung GmbH, Roseggerstraße 12, 8700 Leoben, Austria
² Chair of Metal Forming, Montanuniversitaet Leoben, Franz-Josef-Straße 18, 8700 Leoben, Austria
³ Institute of Mechanics, Montanuniversitaet Leoben, Franz-Josef-Straße 18, 8700 Leoben, Austria
⁴ Chair of Joining, Technische Universität Berlin, Straße des 17. Juni 135, 10512 Berlin, Germany
⁵ Fraunhofer IPK, Pascalstr. 8-9, 10587 Berlin, Germany
⁶ Federal Institute for Materials Research and Testing (BAM), Unter den Eichen 87, 12205 Berlin, Germany
⁷ Mercedes-Benz AG, 71059 Sindelfingen, Germany
⁸ voestalpine Stahl GmbH, voestalpine-Straße 3, 4020 Linz, Austria

Table 1 Chemical composition of the DP1200HD

C (%)	Si (%)	Mn (%)	Fe
0.2	1.5	2.5	Balanced

be found [27]. To mimic the conditions during real-world RSW, it is useful to include lateral mechanical loading of the welded sheets. To gain deeper insights, Frei et al. developed a welding test under external load [28, 29], which includes straining one of the two welded sheets to a fraction of the yield strength. The drawback of such technological test is that the local loading and, thus, the root cause of the effects observed, e.g. LME cracking, remain unknown. Accompanying finite element modelling of the RSW experiments as developed by Prabitz et al. [2, 30–32] allows the evolution of the local physical quantities to be investigated and provides a solution to this issue. This is also key to ensure the transferability of the findings under lab conditions to real-world production.

For the current paper, the test setup for welding under external load was applied to UC and EG DP1200HD steel in order to evaluate their susceptibility to LME. Subsequently, the experiments were modelled by means of a novel fully coupled electrical, thermal, metallurgical and mechanical RSW finite element analysis. In addition, newly developed experimentally based and not in literature found plastic and LME damage indicator concepts were applied to predict embrittlement and predetermine the onset of cracking for both UC and EG steel. The objective with this model is to correctly describe and revise the influence of the sample geometry on the cracking location, which is necessary to compare this testing method with other testing methods. In this vein, the RSW tests performed under external load were evaluated, and the RSW and LME models applied were validated.

2 Methodology

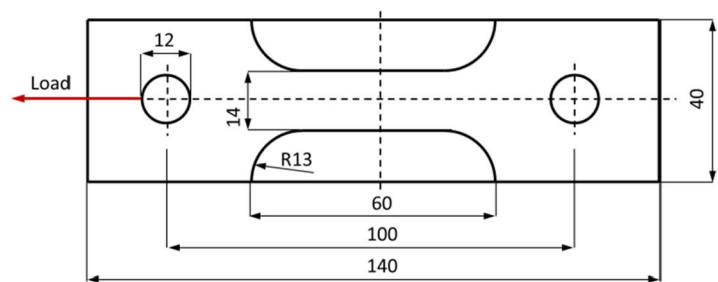
2.1 Experimental

The DP steel investigated had a UTS of 1200 MPa and a yield stress of 1050 MPa and provided high ductility with a fracture strain of 14 % (DP1200HD). Experimentally, the UTS was found to exceed 1400 MPa. The electrogalvanized base material had a bainitic–ferritic microstructure, and the zinc coating layer thickness was about 7 μm . The chemical composition of the DP1200HD is shown in Table 1. In [30], the interested reader can find the material data that builds the foundation of this work.

Dog-bone-shaped samples depicted in Fig. 1b and rectangular samples of dimensions 40 mm by 60 mm, both with a thickness of 1.6 mm, were arranged in a 2-sheet stack-up and welded together in the setup for welding under external load; see Fig. 1a [33]. The UC samples were machined from the same coil as the EG samples, albeit before undergoing the electrolytical zincification process. For welding, a servo-mechanical welding gun with a C-calliper and constant current control was used. The electrode geometry F1-16-20-5.5 with a radiused tip (radius = 50 mm) and a sharp shoulder widely used in the automotive industry was selected for the experiment. For further specifications of the CuCrZr electrodes, see ISO 5821 [34]. The maximum welding current to produce maximum-sized spot welds was determined in accordance with SEP 1220-2 [35]. The lower electrode force was applied as a proactive measure due to the susceptibility to LME cracks. For this purpose, the electrode force (3.5 kN), the welding time (380 ms) and the holding time (300 ms) were fixed, and the current was incrementally increased from 3.0 kA by 200 A steps until spatter occurred. Then, the current was



a)



b)

Fig. 1 a The sample mounted in the welding gear with external load application; b the dog-bone-shaped tensile sample with the applied external load

reduced in increments of 100 A until three consecutive welds remained spatter-free. The current applied during all welding under external load experiments was 6.5 kA. The welding current, originally specified for UC steel, was intentionally applied to EG steel for the purpose of assessing and comparing the surface influence on welding outcomes. This crossover approach aims to provide more insightful and comprehensive findings in understanding the surface-dependent dynamics of the welding process. The prescribed standard electrode force, in accordance with the SEP guidelines, is established at 4.5 kN. Nevertheless, for the present experiment, a deliberate deviation was made, and the electrode force was calibrated to 3.5 kN to align with the specific requirements of the experimental setup. This adjustment was motivated by insights gained from preceding experiments conducted by J. Frei [28, 29, 33]. The primary objective was to facilitate comparability with the outcomes of these prior investigations.

The external load (red arrow in Fig. 1b) was applied displacement controlled until it reached a certain fraction of the yield strength with ascending load increments of 10% yield stress. LR_n describes the nominal loading ration

in % of the yield strength, which was applied for 10%, 20%, 30% and 40% load. Tensile loaded RSW tests are typically ranked by the applied tensile force in % of the yield strength R_{p02} at room temperature [29]. This quantity is called the nominal loading ratio LR_n . The UC samples fractured at 60 % nominal loading ratio LR_n , whereas all but one of the EG samples fractured at 50 % of nominal loading ratio LR_n .

The displacement was applied prior to welding and was kept constant throughout the experiment. For each load increment, ten samples were tested. The highest load level was determined as the point when three consecutive samples broke apart during the welding under external load experiment. For each load step, a longitudinal micrograph through the centre of the weld spot (x - y plane Fig. 2a) was prepared to evaluate crack depths with ImageJ and Fiji [36]. The remaining samples were dezincified with hydrochloric acid and, together with the UC samples, subjected to a dye penetration test under UV light. The length of the digitized surface cracks was further evaluated in the samples top view of the x - z plane (see Fig. 2a) and measured with Fiji. The crack lengths were then averaged.

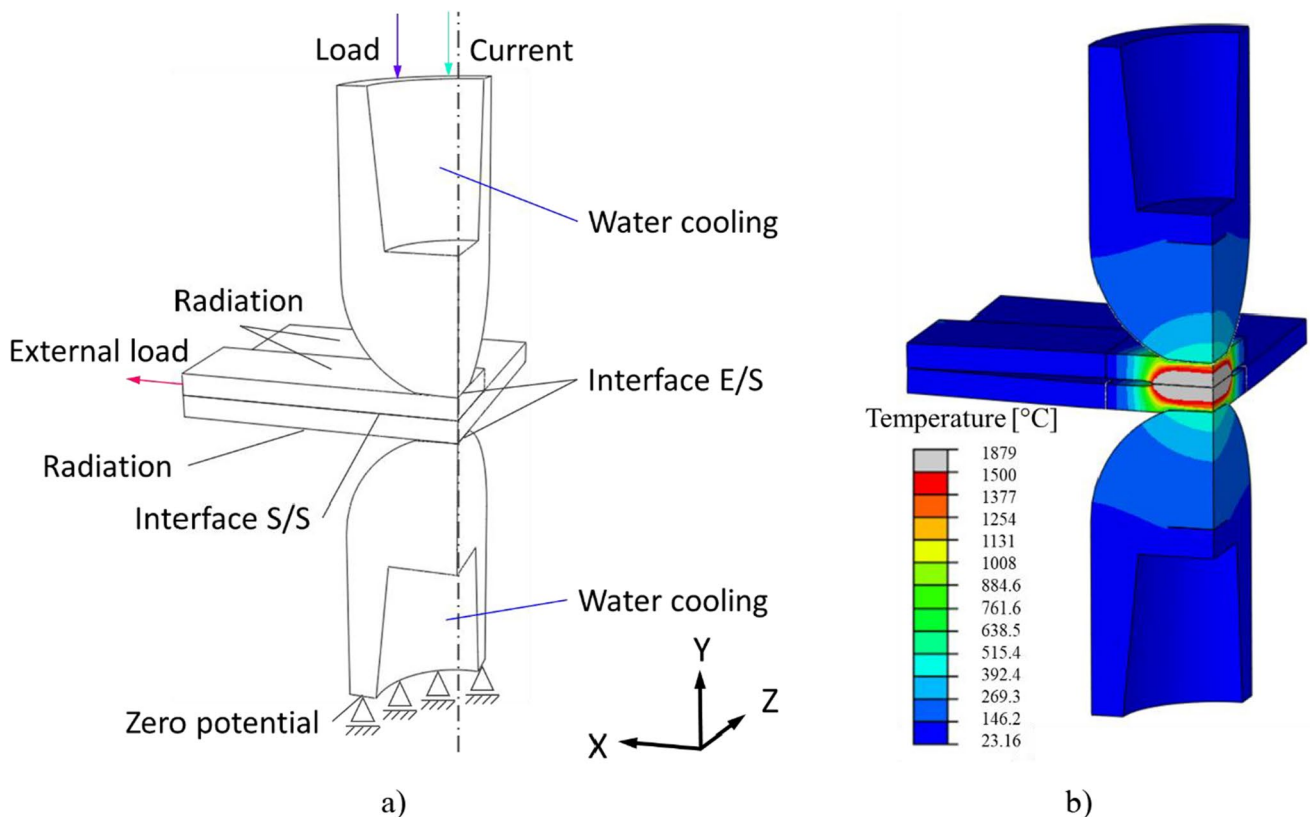


Fig. 2 **a** The schematic welding model with all boundary conditions and loads applied; **b** a typical temperature distribution of a spot weld for 10% of the yield stress applied as external load captured at the end of the welding step

2.2 FE modelling

The evolution of the local physical quantities during RSW was modelled by means of a strongly coupled multi-physical thermal, electrical, mechanical and metallurgical finite element model using the commercial software package Abaqus 2019 [37]. A detailed description of the material model including the complete set of experimentally determined parameters as well as the contact conditions can be found in [30] as well as in Table 2.

Phase transformation phenomena and the dependence of material properties on temperature were taken into account. For the sake of simplicity and convergence reasons, the plastic material data were reduced to the parameter set of the strain rate of 0.1 s^{-1} dominating during RSW [30]. For meshing, hexahedral Q3D8R and wedge Q3D6R elements were chosen.

Figure 2a provides an overview of the loads and boundary conditions applied. For numerical efficiency, the model makes use of a quarter symmetry, and the geometry is truncated such that only the relevant areas of the dog-bone-shaped sample near the welding zone are considered. The load and current density assigned to the top electrode were chosen according to the process parameters used in the experiments. Furthermore, the parameters for the convective water cooling were calculated assuming turbulent flow with a flow rate of 6 l/min and a water temperature of 20 °C. Thermal and electrical contact conditions between the sheet to sheet (S/S) and the electrode to sheet (E/S) interface and the conditions for radiation can be found in a previous publication [30]. The tensile load was applied in the form of a distributed load in positive x -direction — see Fig. 2a — acting on the cutting plane of the dog-bone-shaped sample sufficiently far from the spot weld. Figure 2b shows a typical temperature distribution after

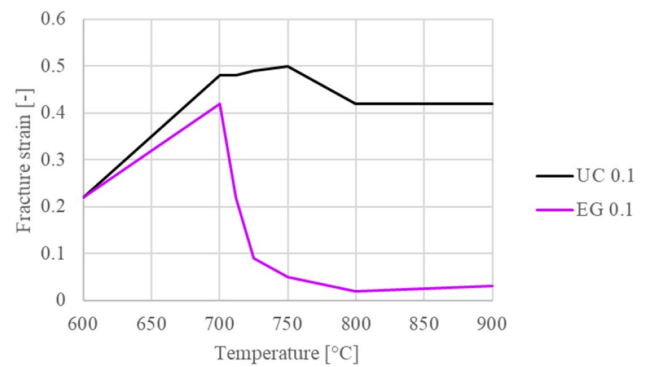


Fig. 3 Reduction of ductility while comparing the fracture strain of hot tensile tests for electrogalvanized (EG) (purple, slashed) and uncoated (UC) steel (black) for a strain rate of 0.1 s^{-1}

the welding process. Investigating temperatures provides insights in critical zones and is mandatory for further calculations.

2.3 Damage indicator

In order to evaluate the local occurrence of LME, an experimentally based semi-empirical damage indicator D_{LME} was developed. For this purpose, isothermal hot tensile tests were carried out on a Gleeble® 3800 for a broad range of strain rates and temperatures using EG and UC DP1200HD samples. The edges of the galvanized steel, which was electrogalvanized on both sides, underwent a polishing process to remove any potential border cracks. Additionally, a thermocouple was carefully welded to one side of the steel sheet. It is important to note that this addition did not affect the liquid metal embrittlement (LME) behaviour observed in the experiments, as crack initiation was uniformly distributed across the entire sample. The results revealed a clear

Table 2 Depicting the contact conditions

T °C	Electrode to sheet contact		Sheet to sheet contact	
	Electrical conductance 1/(mOhm mm ²)	Thermal conductance mW/(mm ² K)	Electrical conductance 1/(mOhm mm ²)	Thermal conductance mW/(mm ² K)
25	2	100.00	0.08	250.0
250	2.6	500.00	0.08	1000.0
350	2.87	725.81	0.08	1225.8
400	3	632.26	0.082	1338.7
420	36	794.84	0.082	1383.9
500	200	980.65	0.085	1564.5
530	220	1050.32	0.086	1632.3
650	220	1329.03	0.09	1903.2
1250	220	2722.58	0.10	3258.1
1500	220	3303.23	0.20	3822.6
1800	220	4000.00	0.20	45000.

dependency of LME on zinc availability, temperature, strain rate and plastic strain. Figure 3 shows the dependency of the fracture strain on the testing temperature for EG and UC material and makes the effect of LME clearly visible. The LME damage indicator D_{LME} is based on a classical ductile damage indication which was extended by some LME-specific expressions. For further details on the damage indicator and for the effect of strain rate on LME, the interested reader is referred to a previous publication [31]. Galvanized steel samples, each measuring 20 mm in width, 1.6 mm in thickness and 45.28 mm in length, were subjected to testing. The samples were subjected to controlled heating at a rate of 300 °C/s, maintained at the specified temperature during deformation, and subsequently conventionally cooled in ambient air.

Since the performance of both UC and EG material is of importance besides the damage indicator for LME D_{LME} [31] in the present paper, a second indicator D_{UC} for the damage evolution of the UC material state was developed. The main structure of this simple, yet sufficiently accurate damage indicator D_{UC} follows the equations describing the LME damage indicator, but the fracture strain ϵ_f was adapted to fit the UC material. $d\epsilon_{pv}$ describes the plastic strain increment. The evaluation was carried out for the predominant strain rate of 0.1 s⁻¹. The governing equation for damage accumulation can be seen in (1), while the experimentally based temperature-dependent formulation of ϵ_f is, together with the temperature T and the corresponding parameters a - e accounting as fit-parameter that are adopted for the fracture strain, given in (2). Note that fracture of the sample is preceded by a small amount of necking. This is disregarded for the determination of ϵ_f . The damage indicator D_{UC} is thus expected to be slightly too conservative:

$$D_{UC} = \int_0^{\epsilon_{pv}} \frac{d\epsilon_{pv}}{\epsilon_f} \quad (1)$$

$$\epsilon_f = a - bT + cT^2 + dT^3 - eT^4, \text{ with} \quad (2)$$

$$\begin{aligned} a &= 1.01 \times 10^{-01} \\ b &= 3.66 \times 10^{-04} \\ c &= 5.80 \times 10^{-07} \\ d &= 4.92 \times 10^{-10} \\ e &= 6.12 \times 10^{-13} \end{aligned}$$

The interested reader can find all equations leading to the damage indicator for EG steel in [31]. There D_{LME} equals D_{UC} , while ϵ_f given in (3), is different for the LME damage indicator (A - E were experimentally defined for EG steel, T_{LME} equals the minimum temperature for LME occurrence, and $\dot{\epsilon}$ describes the strain rate):

$$\epsilon_f = \frac{A}{\frac{B-T_{LME} + \frac{T_{LME}}{\dot{\epsilon}}}{C} + \left((D + T_{LME}) - \frac{E-T_{LME}}{e^{\dot{\epsilon}}} \right)} \quad (3)$$

3 Results

Tensile loaded RSW tests are typically ranked by the applied tensile force in % of the yield strength $R_{p0.2}$ at room temperature [29]. This quantity is called the nominal loading ratio LR_n . The UC samples fractured at 60 % nominal loading ratio LR_n , whereas all but one of the EG samples fractured at 50 % of nominal loading ratio LR_n . Hence, a clear LME effect is seen, but the embrittlement observed at the sample level is less pronounced in this experimental setup as compared to isothermal hot tensile tests [31, 33]. Since the sample width of 14 mm is small in the chosen setup compared to the fusion zone size of about 6 mm [29], the nominal loading ratio LR_n is merely a technological quantity. Since LR_n depends greatly on geometry, it may lead to misinterpretations when related to real loading situations appearing during the welding of components. The model-based evaluation of the experiment allows for defining a more general and better comparable loading quantity, i.e. the geometry-independent nominal loading ratio LR_{in} which relates the maximum longitudinal stress from the sample edge at the length coordinate of the centre of the spot weld to the yield strength at room temperature $R_{p0.2}$. The maximum longitudinal stress values were obtained numerically for the different load levels. In the current case, the geometry-independent nominal loading ratio LR_{in} is significantly larger than the conventional measure LR_n .

The quality of most of the UC weld spots turned out to be good, and only 4 out of 50 samples investigated showed expulsion between the sheets. In contrast, for the EG samples, a major fraction of the welds showed expulsion. The cause was not investigated in this work due focus on LME but might be dependent on high welding currents. In order to exclude the effect of expulsions, only the samples without expulsions were cut for micrographs. Note that due to expulsions, the electrode indentation can increase and cause higher wear of the electrodes, which may produce for non-uniform spot welds. While no surface cracks were found in the UC samples, surface cracks were observed in the EG samples for all load levels. For weld spots without external load, no LME was found. Only 1 ($LR_{in} = 1$) out of all 36 was found to be crack-free. The cracks are located inside the electrode indentation and around the spot weld and can be categorized into four different types depending on location and morphology. In Fig. 4, these types are illustrated and numbered from 1 to 4. The most

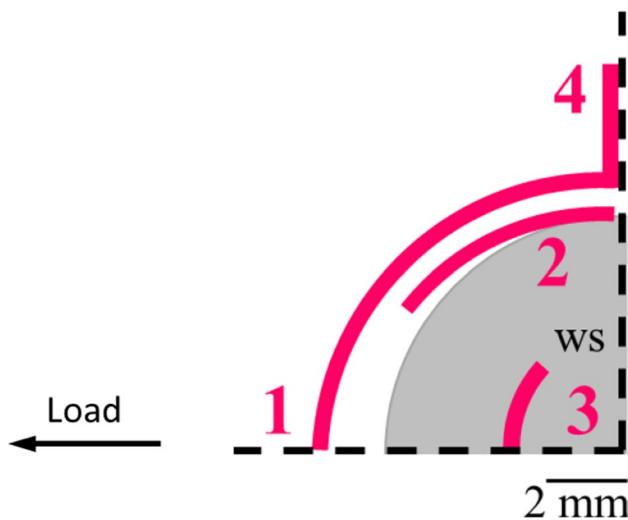


Fig. 4 Schematic top view illustration of the four crack types observed at the spot welds (WS). Positions are indicated in red, while no crack metrics are shown here

common type is found in the circumference of the weld on the higher stressed side of the sample, which corresponds to crack type 1. Type 2 cracks are similar to type 1 but are found closer to the weld centre and do not grow together normal angled to the load direction. They are mainly found at the lowest load level, while type 3 cracks inside the electrode indentation are exclusively seen only once at the lowest load level. For $LR_{in} = 1.26$, two thirds of the welds showed type 4 cracks, which can be explained by a transition from LME cracks to tensile rupture. Type 4 cracks occur radial to the spot weld and normal to the loading direction almost in the transversal symmetry plane of the sample. They are typically not dependent on LME, but due to the inhomogeneous high temperatures and stresses around the spot weld, they are seen in this case as tensile rupture. Hence, the premature failure of the EG material at 50 % yield stress ($LR_{in} = 1.39$) emanates from an interaction of LME damage and high plastic deformations. Note that the load was applied for each sample in the load direction, as seen in Fig. 4.

At $LR_{in} = 0.87$, the dominating crack type is type 2, whereas only few instances of type 1 are found; see Table 3. The total number of cracks across all samples is aggregated,

Table 3 Summary of crack count and crack location as a sum of all samples with the according average crack length and the standard crack length deviation in mm

LR_{in}	LR_n	ct 1	avg	dev	ct 2	avg	dev	ct 3	avg	dev	ct 4	avg	dev
0.87	0.1	5	12.25	1.97	8	4.51	0.85	1	5.66	0			
1.00	0.2	6	8.73	5.07	2	4.01	0.24				3	3.00	1.09
1.13	0.3	8	10.85	0.81	2	4.12	0.55						
1.26	0.4	9	12.42	0.86							11	3.11	1.34

ct crack type, avg average crack length, dev standard deviation of crack length

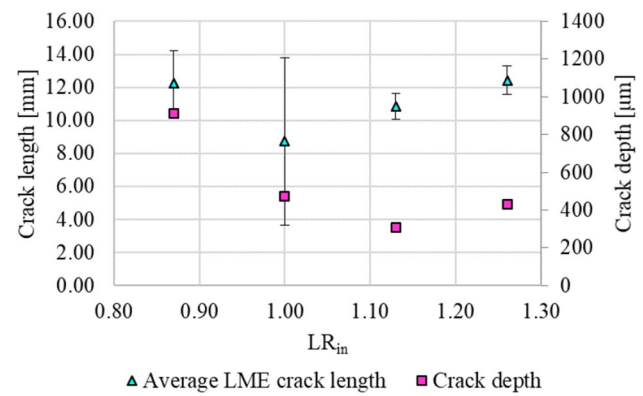


Fig. 5 Comparing the mean surface crack lengths as well as depths measured in micrographs of crack type 1 for all different load levels of EG samples

with type 4 cracks being identified on both sides of the weld spot. For higher loads, type 1 becomes dominant due to the development of plastic strain next to the RSW induced by the external load. Some cracks at location 4 can be found at $LR_{in} = 1$, but most of these cracks occur at the highest load level. This is in accordance with the high load in this area and the induced LME cracks.

Frei et al. [33] published a similar study on spot welding tests under external loading. They investigated a transformation-induced plasticity (TRIP) steel, a microalloyed steel and two complex phase steels. Clearly, this comparably low strength steels showed less susceptibility to LME compared to the DP1200HD investigated in this study, where even at $LR_{in} = 0.87$, cracks were found; see Fig. 5. The scatter of the crack lengths evaluated at different load levels is smaller than that from the tests of Frei et al. [33], and the crack lengths increase with higher external loads but show an anomaly for the lowest load level with highest crack lengths and depths. The crack length is the most important measure in terms of further crack extension in, for example, a crash scenario. In this respect, a very interesting finding is that type 1 LME crack depths tend to decrease with increasing loading. The highest crack depth was found at $LR_{in} = 0.87$ with 911 μm , while the lowest crack depth was 268 μm at $LR_{in} = 1.13$. A possible explanation lies in the stress redistribution after crack initiation and in the lateral crack extension potential due to the loading direction.

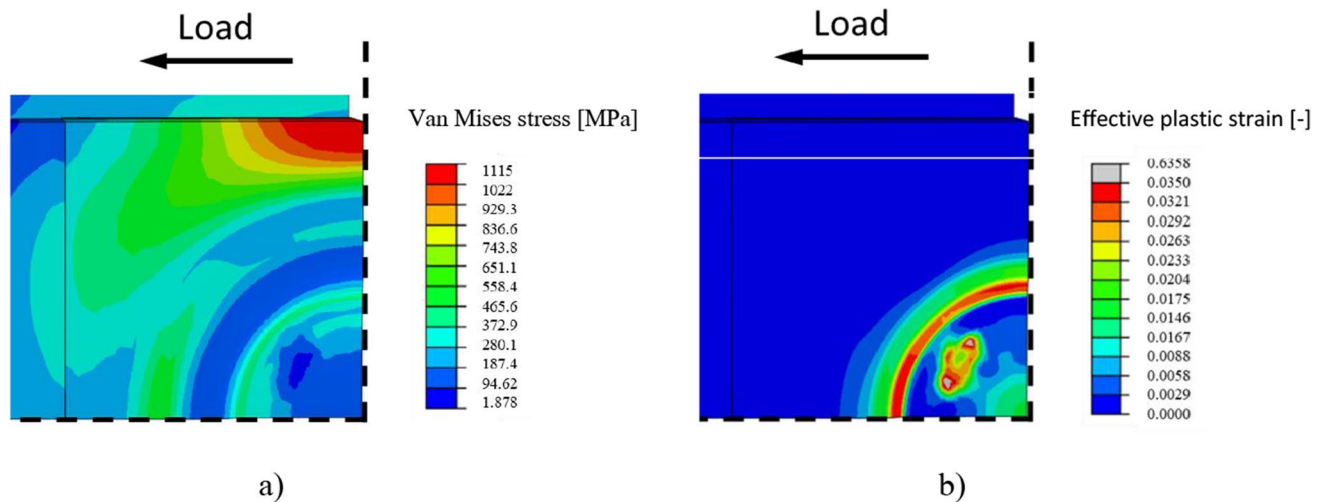


Fig. 6 **a** Von Mises stress and **b** effective plastic strain for a sample with an external load of 10 % yield strength ($LR_{in} = 0.87$) at the end of the heating cycle

The results of the fully coupled multi-physical finite element model serve as a better interpretation of the experimental findings. First, the local deformation and stress state are analysed. Figure 6a shows the von Mises stress state and Fig. 6b the effective plastic strain resulting from a simulation assuming an external load of 10 % yield strength ($LR_{in} = 0.87$) at the end of the heating cycle. Due to symmetry reasons, only a quarter of the sample is exhibited. The highest stresses occur at the long edge of the sample next to the spot weld. The stress increase is on one side due to the lower temperature and, hence, higher yield strength compared to the weld spot region and the other side due to a stress concentration stemming from the reduced load bearing capacity in the spot weld region. Hence, the predominant factor influencing these effects stems primarily from the elevated temperatures present at the weld spot. This stress concentration is the reason for the type 4 cracks leading to the final rupture of the sample. However, in the depicted case of 10 % loading, the highest plastic deformations are situated on the circumference of the spot weld, with the location of the maximum strain close to the axis of the sample. This is a consequence of the externally applied longitudinal load leading to stresses which are superimposed on the eigenstresses resulting from the spot welding. This local strain concentration is the reason for type 1 cracks. Due to the lowest loading level, this strain concentration is clearly less pronounced than for other load levels, which explains that for this case, the mainly eigenstress-driven type 2 cracks also occur.

The damage indicators provide a quantitative picture of the localization of damage. It is important to mention that damage is integrated into the model in an uncoupled way. For the sake of simplicity, the fact that damage may influence the mechanical material properties such as modulus

of elasticity or yield strength was not considered in this case. The mechanical damage indicator D_{UC} becomes higher than 1 after the application of 30 % of the yield strength ($LR_{in} = 1.13$), while the LME damage indicator D_{LME} already exceeds 1 when applying 10 % of the yield stress ($LR_{in} = 0.87$). A damage value above 1 is seen as critical damage leading to crack initiation and elongation, as found in previous experiments [31]. No damage occurs if D_{LME} equals 0. Due to the simplifications regarding the fracture strain ϵ_f mentioned above, the mechanical damage indicator D_{UC} was expected to be conservative. In Fig. 7, we compare D_{LME} with D_{UC} at the instant D_{LME} succeeds critical with the according photographed crack pattern recorded after welding. Figure 7a shows the LME damage indicator D_{LME} for $LR_{in} = 0.87$ at the instant D_{LME} exceeds 1, which happens during holding at a holding time of 5.8 ms. The onset of cracking is predicted by the model in the same position as in the spot weld. An interesting result is that in the area of crack type 2, both the highest damage value and the largest extension of the critical area are indicated. This compares well with the occurrence of crack type 2 especially at this loading level, and it also explains that the location of this crack type is more central, i.e. in a smaller radial position of the spot weld compared to crack type 1. D_{UC} shows no critical values in this configuration. Figure 7b again shows the LME damage indicator D_{LME} , which represents well the crack in the experiment for $LR_{in} = 1.13$ at a welding time of 357 ms. The starting location of the LME crack is shifted here to be crack type 1, which is also reflected by the corresponding image of the dye penetrated surface. At this specific time, D_{UC} does not reach the critical damage level. For $LR_{in} = 1.26$ in Fig. 7c, the LME damage starts at position 1 during the welding

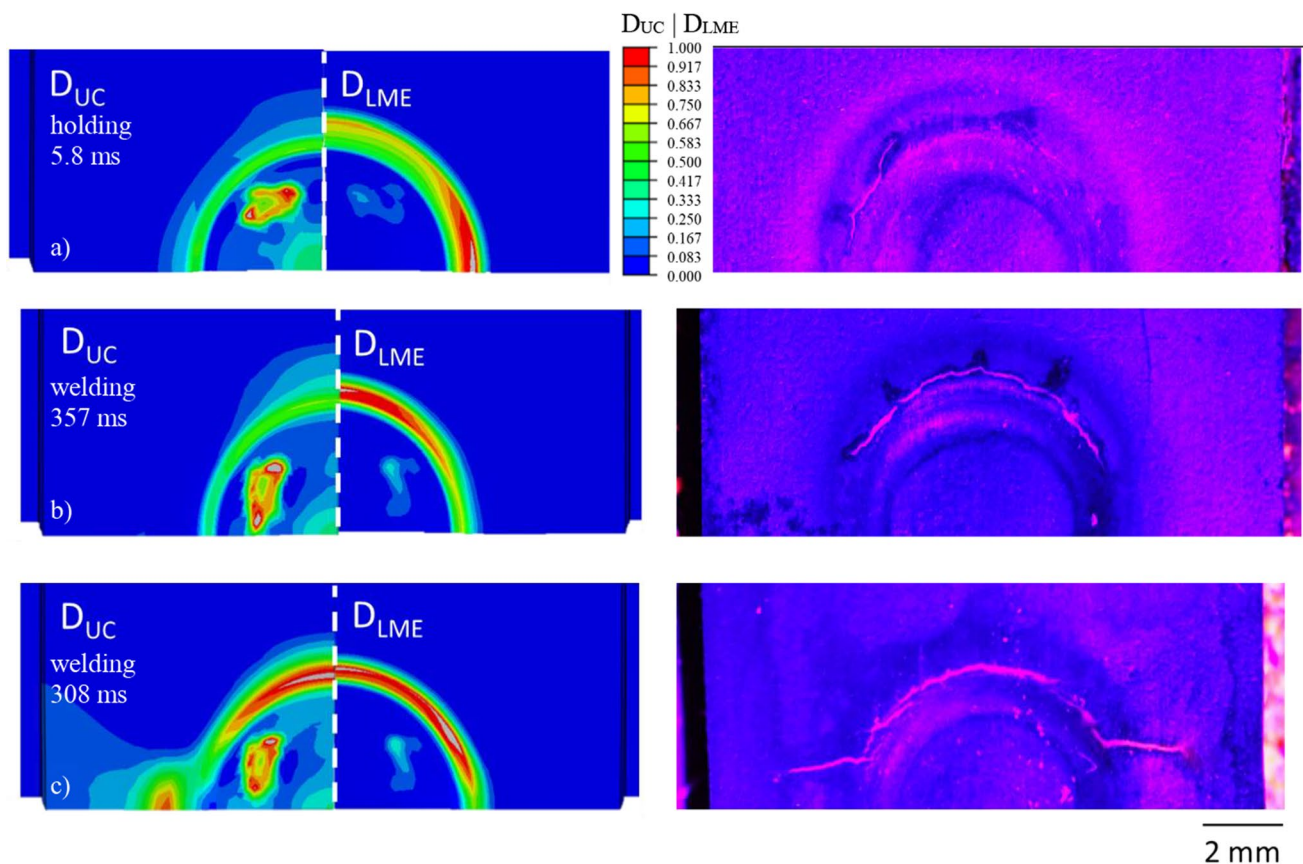


Fig. 7 The modelled LME damage indicator (D_{LME}) is compared to the damage indicator for uncoated material (D_{UC}) (left) at the time D_{LME} first exceeds 1. The corresponding surface pictures (right) reflect the according cracks after welding. For model a with 10 % yield stress ($LR_{in} = 0.87$, 5.8 ms into holding), the LME damage

indicator shows as in **b** with 30 % yield stress ($LR_{in} = 1.13$, 357 ms into welding) the starting location of the crack. **c** With 40 % yield stress ($LR_{in} = 1.26$, 308 ms into welding), an interaction of LME and plastic damage occurs. The cracking patterns seen in the model are reflected by the experiments

at a time of 308 ms. The newly formed cracks at position 4 add to the initial LME cracks but do not cause complete failure. This cracking location is also seen at higher loads where the ultimate rupture is a coupled effect of embrittlement and additional plastic deformation. For the different loading scenarios, the damage indicator predicts crack initiation and crack types very well.

4 Conclusion

Based on the welding under external load experiments and the corresponding finite element modelling of the welding process, the following conclusions can be drawn:

- The welding under external load experiments are an appropriate method to compare the susceptibility of third-generation advanced high-strength steels to liquid metal embrittlement compared to the according uncov-

ered steel grade. In literature, the comparison between steel grades was shown successfully by these experiments. However, for the evaluation of local field quantities and for the purpose of finding their correlation with realistic loading states in actual welded components, accompanying finite element simulations are recommended.

- For the dual-phase steel susceptible to liquid metal embrittlement studied, surface cracks formed in the galvanized state at all tested load levels. Sample fracture occurred in both the galvanized and uncovered state well above a geometry standard with corrected geometry.
- In the symmetry cross-section perpendicular to the loading direction of the samples, a specific loading situation occurred, leading to an influence of plastic damage in addition to the LME damage. Therefore, an optimized sample geometry with an increased width might help to improve the findings.
- The mechanical loading and the predominant strain rate mainly influence the morphology of the liquid metal

embrittlement cracks formed and not in that extend their formation. The prevalence of brittle fracture of galvanized steel and, respectively, plastic fracture of uncoated steel are the main influences on the crack morphology. A remarkable finding is that with increasing external load, the length of the type 1 crack also increases, but the depth most important for the integrity of the joint decreases. Contrary for the lowest load levels, high crack lengths and depths were found.

- The finite element model developed predicts the onset of liquid metal embrittlement cracks and the ductile damage mechanism very well and provides an explanation of the mechanical conditions that lead to crack formation. The evolution of ductile damage is overpredicted due to simplifications in the formulation of the damage indicator which was, however, not the main focus of the current work.

Funding Open access funding provided by Montanuniversität Leoben. The authors gratefully acknowledge the financial support under the scope of the COMET programme within the K2 Center “Integrated Computational Material, Process and Product Engineering (IC-MPPE)” (Project No 886385). This programme is supported by the Austrian Federal Ministries for Climate Action, Environment, Energy, Mobility, Innovation and Technology (BMK) and for Labour and Economy (BMAW), represented by the Austrian Research Promotion Agency (FFG), and the federal states of Styria, Upper Austria and Tyrol.

Declarations

Conflict of interest The authors declare no competing interests.

Open Access This article is licensed under a Creative Commons Attribution 4.0 International License, which permits use, sharing, adaptation, distribution and reproduction in any medium or format, as long as you give appropriate credit to the original author(s) and the source, provide a link to the Creative Commons licence, and indicate if changes were made. The images or other third party material in this article are included in the article’s Creative Commons licence, unless indicated otherwise in a credit line to the material. If material is not included in the article’s Creative Commons licence and your intended use is not permitted by statutory regulation or exceeds the permitted use, you will need to obtain permission directly from the copyright holder. To view a copy of this licence, visit <http://creativecommons.org/licenses/by/4.0/>.

References

- Ashiri R, Shamanian M, Salimijazi HR, Haque MA, Bae JH, Ji CW, Chin KG, Do Park Y (2016) Liquid metal embrittlement-free welds of Zn-coated twinning induced plasticity steels. *Scr Mater* 114:41–47. <https://doi.org/10.1016/j.scriptamat.2015.11.027>
- Prabitz KM, Ecker W, Borchert M, Antretter T, Schubert H, Hilpert B, Gruber M, Sierlinger R (2019) Multiphysics finite element simulation of resistance spot welding to evaluate liquid metal embrittlement in advanced high strength steels. *Math Model Weld Phenom* 12(12):783–793. <https://doi.org/10.3217/978-3-85125-615-4-40>
- Jung G, Woo IS, Suh DW, Kim SJ (2016) Liquid Zn assisted embrittlement of advanced high strength steels with different microstructures. *Met Mater Int* 22:187–195. <https://doi.org/10.1007/s12540-016-5579-7>
- Beal C, Kleber X, Fabregue D, Bouzekri M (2012) Embrittlement of a zinc coated high manganese TWIP steel. *Mater Sci Eng A* 543:76–83. <https://doi.org/10.1016/j.msea.2012.02.049>
- Murugan SP, Jeon JB, Ji C, Park Y (2020) Liquid zinc penetration induced intergranular brittle cracking in resistance spot welding of galvanized advanced high strength steel. <https://doi.org/10.1007/s40194-020-00975-3>
- Scheiber D, Prabitz KM, Romaner L, Ecker W (2020) The influence of alloying on Zn liquid metal embrittlement in steels. *Acta Mater*. <https://doi.org/10.1016/j.actamat.2020.06.001>
- Beal C, Kleber X, Fabregue D, Bouzekri M (2011) Liquid zinc embrittlement of a high-manganese content TWIP steel:0839. <https://doi.org/10.1080/09500839.2011.559177>
- Sierlinger R, Gruber M (n.d.) A cracking good story about liquid metal embrittlement during spot welding of advanced high strength steels, White Pap. Voestalpine Stahl GmbH
- Hamouche-Hadjem Z, Auger T, Guillot I, Gorse D (2008) Susceptibility to LME of 316L and T91 steels by LBE: effect of strain rate. *J Nucl Mater* 376:317–321. <https://doi.org/10.1016/j.jnucmat.2008.02.031>
- Ersoy F, Verbeken K, Gavrilo S (2021) Influence of displacement rate and temperature on the severity of liquid metal embrittlement of T91 steel in LBE. *Mater Sci Eng A* 800:140259. <https://doi.org/10.1016/j.msea.2020.140259>
- Razmpoosh MH, Macwan A, Goodwin F, Biro E, Zhou Y (2020) Materialia Suppression of liquid-metal-embrittlement by twin-induced grain boundary engineering approach. *Materialia* 11:100668. <https://doi.org/10.1016/j.mta.2020.100668>
- Bhattacharya D, Cho L, van der Aa E, Pichler A, Pottore N, Ghassemi-Armaki H, Findley KO, Speer JG (2021) Influence of the starting microstructure of an advanced high strength steel on the characteristics of Zn-assisted liquid metal embrittlement. *Mater Sci Eng A* 804:140391. <https://doi.org/10.1016/j.msea.2020.140391>
- J. Barthelmie, A. Schram, V. Wesling, Liquid metal embrittlement in resistance spot welding and hot tensile tests of surface-refined TWIP steels, 18th Chemnitz Seminar. *Mater. Eng. - 18. Werkstofftechnisches Kolloquium*. (2016) 1–8. doi:<https://doi.org/10.1088/1757-899X/118/1/012002>.
- Prabitz KM, Ecker W, Antretter T, Beal C, Schubert H, Hilpert B, Gruber M, Sierlinger R (2021) Numerical model for predicting liquid metal cracking during resistance spot welding of advanced high strength steels, in: 12th Int. Conf Zinc Alloy Coat Steel Sheet GALVATECH 2020:12
- Dai Y, Long B, Groeschel F (2006) Slow strain rate tensile tests on T91 in static lead-bismuth eutectic. *J Nucl Mater* 356:222–228. <https://doi.org/10.1016/j.jnucmat.2006.05.039>
- Legris A, Nicaise G, Vogt JB, Focit J (2002) Liquid metal embrittlement of the martensitic steel 91: influence of the chemical composition of the liquid metal. Experiments and electronic structure calculations. *J Nucl Mater* 301:70–76. [https://doi.org/10.1016/S0022-3115\(01\)00730-9](https://doi.org/10.1016/S0022-3115(01)00730-9)
- Beal C, Kleber X, Fabregue D, Bouzekri M (2012) Embrittlement of a high manganese TWIP steel in the presence of liquid zinc. *Mater Sci Forum* 706–709:2041–2046. <https://doi.org/10.4028/www.scientific.net/MSF.706-709.2041>
- Ling Z, Wang M, Kong L, Chen K (2020) Towards an explanation of liquid metal embrittlement cracking in resistance spot welding of dissimilar steels. *Mater Des* 195:109055. <https://doi.org/10.1016/j.matdes.2020.109055>

19. He J, Sirois D, Wikle C, Chin B (2019) Weld interface characteristics in ballistic spin impact stud welding of copper to low carbon steel
20. Böhne C, Meschut G, Biegler M, Frei J, Rethmeier M (2020) Prevention of liquid metal embrittlement cracks in resistance spot welds by adaption of electrode geometry. *Sci Technol Weld Join* 25:303–310. <https://doi.org/10.1080/13621718.2019.1693731>
21. Böhne C, Meschut G, Biegler M, Rethmeier M (2020) Avoidance of liquid metal embrittlement during resistance spot welding by heat input dependent hold time adaption. *Sci Technol Weld Join* 0:617–624. <https://doi.org/10.1080/13621718.2020.1795585>
22. DiGiovanni C, He L, Pistek U, Goodwin F, Biro E, Zhou NY (2020) Role of spot weld electrode geometry on liquid metal embrittlement crack development. *J Manuf Process* 49:1–9. <https://doi.org/10.1016/j.jmapro.2019.11.015>
23. Murugan SP, Mahmud K, Ji C, Jo I, Park Y (2019) Critical design parameters of the electrode for liquid metal embrittlement cracking in resistance spot welding. *Weld World*. <https://doi.org/10.1007/s40194-019-00797-y>
24. Choi DY, Sharma A, Ho S, Jae U, Jung P (2018) Liquid metal embrittlement of resistance spot welded 1180 TRIP steel: effect of electrode force on cracking behavior. *Met Mater Int*. <https://doi.org/10.1007/s12540-018-0180-x>
25. Ling Z, Chen T, Kong L, Wang MIN, Pan HUA (2019) Liquid metal embrittlement cracking during resistance spot welding of galvanized Q & P980 Steel. *Metall Mater Trans A* 50:5128–5142. <https://doi.org/10.1007/s11661-019-05388-6>
26. DiGiovanni C, Bag S, Mehling C, Choi KW, Macwan A, Biro E, Zhou NY (2019) Reduction in liquid metal embrittlement cracking using weld current ramping. *Weld World* 63:1583–1591. <https://doi.org/10.1007/s40194-019-00790-5>
27. Wintjes E, Digiovanni C, Biro E (2019) Quantifying the link between crack distribution and resistance spot weld strength reduction in liquid metal embrittlement susceptible steels Quantifying the link between crack distribution and resistance spot weld strength reduction in liquid metal embrit. *Weld World*. <https://doi.org/10.1007/s40194-019-00712-5>
28. Frei J, Biegler M, Rethmeier M, Böhne C, Frei J, Biegler M (2019) Investigation of liquid metal embrittlement of dual phase steel joints by electro-thermomechanical spot-welding simulation electro-thermomechanical spot-welding simulation. *Sci Technol Weld Join*:1718. <https://doi.org/10.1080/13621718.2019.1582203>
29. Frei J, Rethmeier M (2018) Susceptibility of electrolytically galvanized dual-phase steel sheets to liquid metal embrittlement during resistance spot welding. *Weld World*:1031–1037. <https://doi.org/10.1007/s40194-018-0619-1>
30. Prabitz KM, Pichler M, Antretter T, Schubert H, Hilpert B, Gruber M, Sierlinger R, Ecker W (2021) Validated multiphysical finite element modelling of the spot welding process of the advanced high strength steel DP1200HD. *Materials* 14. <https://doi.org/10.3390/ma14185411>
31. Prabitz KM, Asadzadeh MZ, Pichler M, Antretter T, Beal C, Schubert H, Hilpert B (2021) Liquid metal embrittlement of advanced high strength steel: experiments and damage modelling. *Materials* 14. <https://doi.org/10.3390/ma14185451>
32. K.M. Prabitz, T. Antretter, H. Schubert, B. Hilpert, M. Gruber, R. Sierlinger, M. Mark, S. Seibold, W. Ecker, Novel microalloying and electrode solutions to avoid liquid metal embrittlement during resistance spot welding of galvanized DP1200HD steel, in: 6th Int. Conf. Steels Cars Truck., 2022
33. Frei J, Suwala H, Rethmeier M, Frei MSJ (2016) Bestimmung der Rissanfälligkeit von hochfesten Stählen beim Widerstandspunktschweißen. *Mater Test* 58:7–8
34. Deutsches Institut für Normung (DIN), DIN EN ISO 5821:2010. Resistance welding – Spot welding electrode caps., (2010)
35. SEP 1220-2:2011 testing and documentation guideline for the joinability of thin sheet of steel – part 2: resistance spot welding, Stahlinstitut VDEh. (2011)
36. Schindelin J, Arganda-Carreras I, Frise E, Kaynig V, Longair M, Pietzsch T, Preibisch S, Rueden C, Saalfeld S, Schmid B, Tinevez J-Y, White DJ, Hartenstein V, Eliceiri K, Tomancak P, Cardona A (2012) Fiji: an open-source platform for biological-image analysis. *Nat Methods* 9:676–682. <https://doi.org/10.1038/nmeth.2019>
37. Dassault Systems Simulia Corp., ABAQUS 2019 (2019) <https://www.3ds.com/de/produkte-und-services/simulia/produkte/abaqus/>

Publisher's Note Springer Nature remains neutral with regard to jurisdictional claims in published maps and institutional affiliations.